

## Article

# Blade Design and Aerodynamic Performance Analysis of a 20 MW Wind Turbine for LCoE Reduction

Kang-Ho Jang <sup>1</sup> and Ki-Wahn Ryu <sup>2,\*</sup>

<sup>1</sup> Department of Aerospace Engineering, Graduate School, Jeonbuk National University, 567 Baekje-daero, Deokjin-gu, Jeonju 54896, Jeonbuk, Republic of Korea; all3602zz@naver.com

<sup>2</sup> Department of Aerospace Engineering, Jeonbuk National University, 567 Baekje-daero, Deokjin-gu, Jeonju 54896, Jeonbuk, Republic of Korea

\* Correspondence: kwryu@jbnu.ac.kr; Tel.: +82-63-270-4286

**Abstract:** The aim of this study is to develop a blade mass model that incorporates a low-induction rotor (LIR) and a low-specific power concept to reduce aerodynamic loads and lower the Levelized Cost of Energy (LCoE). This blade mass model replaces the traditional simple scaling rule and incorporates the concept of LCoE reduction, presenting not only the mass distribution in the blade span direction but also the stiffness distribution. In order to achieve the desired reduction in LCoE, we developed a mathematical model that expresses blade mass as a function of the axial induction factor, which influences the aerodynamic load on the blade. We used this model to determine geometries of various low-induction rotors for 20 MW class horizontal axis wind turbine, and to identify the axial induction factor that correlates with the lowest blade mass. The chord length and twist angle in the spanwise direction of the blade were determined using PROPID's reverse design process, based on the specified axial induction factor. Since the low-induction concept is not aerodynamically optimal, a low-specific power design approach was also adopted. This involved increasing the blade length and shifting the power curve to the left. By doing so, the AEP is increased, directly contributing to a reduction in the LCoE. Mass per unit length of the blade was presented, reflecting the distribution of airfoil type, blade geometry, and shapes of internal structures such as spars and webs.

**Keywords:** axial induction factor; blade element momentum theorem; blade mass model; levelized cost of energy; low-induction rotor; low-specific power; preliminary design



**Citation:** Jang, K.-H.; Ryu, K.-W. Blade Design and Aerodynamic Performance Analysis of a 20 MW Wind Turbine for LCoE Reduction. *Energies* **2023**, *16*, 5169. <https://doi.org/10.3390/en16135169>

Academic Editor: Abu-Siada Ahmed

Received: 27 May 2023

Revised: 25 June 2023

Accepted: 3 July 2023

Published: 5 July 2023



**Copyright:** © 2023 by the authors. Licensee MDPI, Basel, Switzerland. This article is an open access article distributed under the terms and conditions of the Creative Commons Attribution (CC BY) license (<https://creativecommons.org/licenses/by/4.0/>).

## 1. Introduction

The global need for new research and development of large-scale wind turbines is growing. New wind turbines will help lower the Levelized Cost of Energy (LCoE) [1], and efficiently harness the powerful and renewable energy source that is wind. Wind turbine manufacturers such as Vestas, Siemens-Gamesa, GE, and Mingyang have already commercialized or are preparing to commercialize 12 to 16 MW wind turbines, and national institutions are also actively researching the topic. The US National Renewable Energy Laboratory (NREL), for example, announced a 5 MW reference wind turbine (RWT) [2] in 2009. Although the NREL 5 MW wind turbine was not intended for manufacture, it was used to provide input data for FAST software version 7 [3] (an aeroelastic analysis tool for wind turbines) and served as a widely known reference among wind turbine manufacturers as well as researchers. The IEA presented a 15 MW class wind turbine [4], which was scaled-up based on a DTU 10 MW reference wind turbine [5], and also presented related aeroelastic analysis results using HAWC2 software version 12.8 [6] developed by DTU. The DTU 10 MW system adopted a medium speed multi-stage gearbox with a maximum tip speed of 90 m/s, whilst the IEA 15 MW system adopted a direct drive and had maximum tip speed of 95 m/s. The two systems were identical in their other parameters, as both belonged to the FFA-W3 airfoil series, IEC-1B turbine class, and possessed the same upwind-type rotor orientation and three-bladed rotor.

Reference [5] reports a 3-bladed 20 MW upwind rotor system based on the UpWind 5-MW reference turbine (version 8). The design employed the ECN's PHATAS code for aeroelastic load calculation consistent with IEC61400-1 edition 2 Class II B [7]. Blade shape was determined using the classically up-scaled wind turbine geometry in BOT [8]. High Reynolds number aerodynamic performance data up to 20 million was investigated using RFOIL [9]. Other 20 MW wind turbines have been developed and presented through Up-Wind, INNWIND.EU, and other projects for reference wind turbines [10,11]. Furthermore, a phased study for the development of a 50 MW class wind turbine system is in progress in the United States of America [12–15].

The INNWIND.EU project of the European Union has developed innovative rotor designs, drivetrain components, and fixed and floating substructures that significantly reduce the LCoE (levelized cost of energy) while increasing the efficiency of 10 and 20 MW offshore wind turbines [16]. One of the project's most important innovations is the low axial induction rotor (LIR), which captures more energy while constraining extreme loads at the blade root and large rotor diameters [16,17]. During the blade design stage, the amount of material used in the blade is the most significant cost determinant. Scaling up a 5 MW class wind turbine to a 20 MW class turbine results in a doubling of blade length, but an eight-fold increase in mass [1,18]. Unfortunately, the new generation of improved materials used for wind turbine manufacturing has not kept pace with the speed of load increase associated with larger wind turbines. To reinforce the stiffness of the blades, using more material may be necessary, which increases the LCoE. Therefore, an additional consideration in the design of very large blades, such as those in the 20 MW class, is how to reduce loads while meeting power curve requirements. To address these issues, the concept of low-induction rotor design has been introduced. The axial induction factor is the fractional decrease in axial wind speed between the far upstream and rotor plane, and the lower the axial induction factor, the less thrust is produced. The INNWIND.EU's 20 MW LIR blade is 13% longer and 7.6% heavier than the blade of the 20 MW reference wind turbine developed through the same project [17]. Ultimately, the LCoE was reduced by 4% using this system instead of the 20 MW RWT [17].

One study attempted to obtain the lowest LCoE possible by changing the number of blades, tip speed ratio, chord length distribution, axial induction factor, and lift coefficient of 20 MW or higher-class reference wind turbines. Clearly, achieving a lower LCoE is a very important goal, even at the preliminary design stage. While estimating annual energy production during this stage is not difficult, estimating the production costs, a component of LCoE, requires a study. LCoE can be divided into two topics: wind turbines and wind farms. Shafiee et al. [19] developed a parametric whole life cycle cost model to identify the key cost drivers of offshore wind projects and parameters that significantly influence the LCOE. The proposed model was tested on a 500-MW offshore baseline wind farm project, and the results were compared with experimental findings reported in the literature. It is asserted that the proposed model can help evaluate project performance and reduce costs. Griffith et al. [20] studied blade manufacturing costs for the Sandia 100 m wind turbine blade using the Sandia Blade Manufacturing Cost Tool (version 1.0). They conducted sensitivity studies as examples to demonstrate the potential use of the tool for cost tradeoff analyses between materials, labor content, and equipment components involved in blade manufacturing. Ashuri [21] and Ashuri et al. [22] presented a method for multidisciplinary design analysis optimization (MDAO) of large-scale wind turbines. In their referenced work, they optimized the NREL 5 MW reference wind turbine and scaled it up to 10 MW and 20 MW to evaluate the effect on LCoE. Rotor and tower design parameters were optimized with the goal of reducing LCoE. In particular, the results obtained from the study of Reference [21] were used to identify the scaling rule tendency. Serafeim et al. [23] proposed an MDAO approach to reduce the LCoE of the DTU-10 MW Reference Wind Turbine. A cost model for the entire wind turbine was implemented by combining existing models from the literature with open data. The model considers the costs of composites, resin, adhesive, paint, bolts, lightning protection, as well as labor and other manufacturing

process expenses. In addition, Bortolotti et al. [24] presented several other MDAO-based frameworks. In their study, they described a comprehensive blade cost model for wind turbine blades ranging from 30 to 100 m in length. The proposed cost model was applied to three specific blades: the WindPACT blade, the IEA 3.4 MW wind turbine blade, and the SNL-100-03 blade. Material costs accounted for 45–70% of the total cost of these three blades [20,24].

In this study, the LCoE calculation focuses specifically on wind turbines. The cost elements of a wind turbine, as identified in Fingersh et al.'s study [1], include the rotor, tower, drive train and nacelle, control and safety system, and balance of station. Additionally, for offshore wind turbines, there are supplementary costs associated with factors such as marinization, scour protection, and port and staging equipment. The most important elements of a wind turbine are the blade diameter and tower height. Cost of blade and tower account for 30% of the total cost [22].

The reasons for presenting the blade mass model in this study and the need for it are as follows. Firstly, the proposed blade mass model replaces the traditional simple scaling rule [1,21] and incorporates the concept of reducing LCoE. It can provide not only mass distribution along the blade span but also the stiffness distribution. A low-induction rotor and a low-specific power [25] concepts were adopted to reduce aerodynamic loads and lower the LCoE. The low-induction rotor design reduces the aerodynamic force exerted on the blade by minimizing the axial induction factor, resulting in a decreased amount of material required for blade fabrication. Additionally, the low-induction factor design compensates for lower power by increasing the blade length, achieving a low specific power and enabling the generation of rated power at lower wind speeds. This adjustment shifts the P-V curve to the left, ultimately increasing annual power generation. Moreover, by finding the axial induction factor that minimizes mass while satisfying the given P-V curve, the chord length and twist angle of the blade can be determined. The reduction in blade mass and the subsequent increase in annual energy production directly contribute to a lower LCoE, not only for the designed blade but also for the entire wind turbine system. Blade shapes, performance curves, and flapwise bending moments for various axial induction factors at the blade root are compared. Finally, the mass model of the blade proposed in this study can be used to obtain blade data for comprehensive aeroelastic analysis tools such as FAST [3], including mass and stiffness distributions along the span direction. It is important to note that these blade data already reflected the concept of reducing the LCoE of the wind turbine in an earlier step of the MDAO process.

## 2. The Idea of the Low-Induction Rotor

The relationship between the mass model and the axial induction factor was determined using blade element momentum theorem [26]. In this theorem, a one-dimensional incompressible steady potential flow is assumed. The rotor and its surrounding flow were briefly modeled with a stream tube (Figure 1). The axial induction factor  $a = (V_0 - u)/V_0$  was defined using the free stream wind speed  $V_0$  and wind speed  $u$  at the rotor plane. The power coefficient and thrust coefficient, which are the main coefficients of the wind turbine, were expressed as the axial induction factor. An optimal aerodynamic design aims to have an axial induction factor of  $a = 1/3$  with a maximum power coefficient. As shown in Figure 2, as the axial induction factor was reduced from  $1/3$  to  $1/4$ , thrust decreased by 16%, while power decreased by only 5%, i.e., thrust materially decreased whilst the power decreased only slightly. The low-induction rotor design, which reduces the aerodynamic loads acting on the blade, reflects this idea. Equations (1) and (2) are the power and thrust coefficients for one-dimensional axisymmetric flow, expressed as an axial induction factor using the 1D momentum theorem:

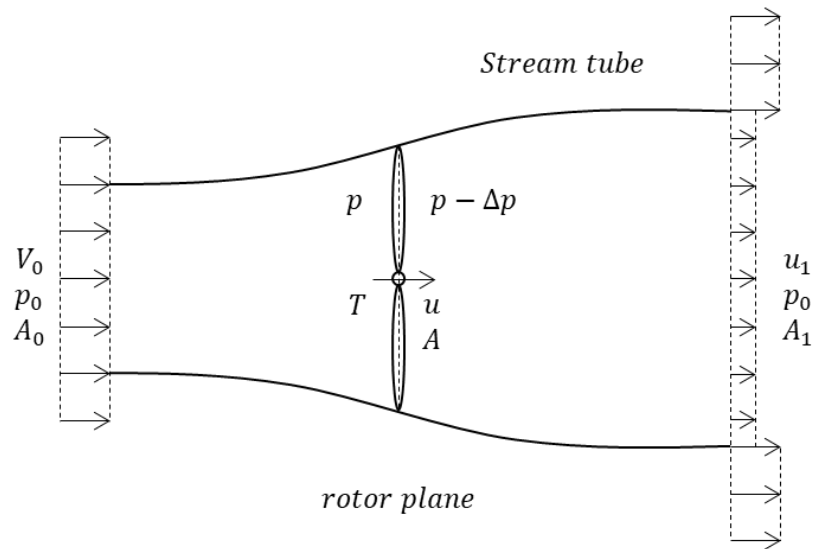


Figure 1. Control volume around a horizontal axis wind turbine.

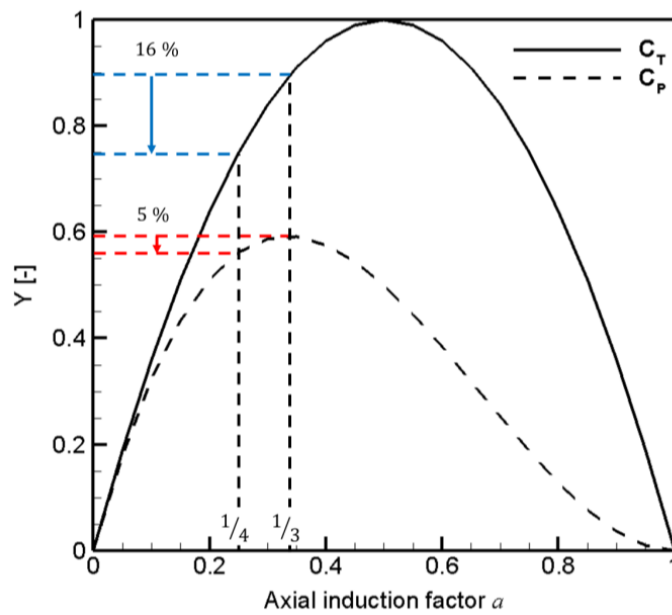


Figure 2.  $C_T$  and  $C_P$  vs. axial induction factor  $a$ .

$$C_P = 4a(1 - a)^2 \tag{1}$$

$$C_T = 4a(1 - a) \tag{2}$$

This time, we want to determine the thrust acting on the blade using the blade element momentum theorem. Figure 3 illustrates the aerodynamic loads acting on a blade section located at a distance of  $r$  from the rotating axis and rotating at a speed of  $\omega$ . Relative wind  $V_{rel}$  brought to the cross section of the wind turbine blade and the components of the decomposed forces.  $D'$  and  $L'$  represent drag and lift, while  $T'$  and  $H'$  represent the results of decomposition into the thrust in a direction perpendicular to the rotor plane and the tangential force applied to the rotor plane.  $H'$  directly affects power by inducing torque, while  $T'$  affects the bending moment of the blade. All forces were assessed in terms of [Newton/m]. According to the momentum theorem, power is a function of axial and

tangential induction factors, but thrust is a function of only the axial induction factor. This is expressed as the following equation:

$$T' = 4\pi\rho V_0^2 a(1-a)r/B \quad (3)$$

in which  $B$  denotes the number of blades. The reduced power, a function of the low-induction rotor design, was compensated for by increasing the length of the blade. All blade designs were compared and analyzed based on the same power curve assumptions.

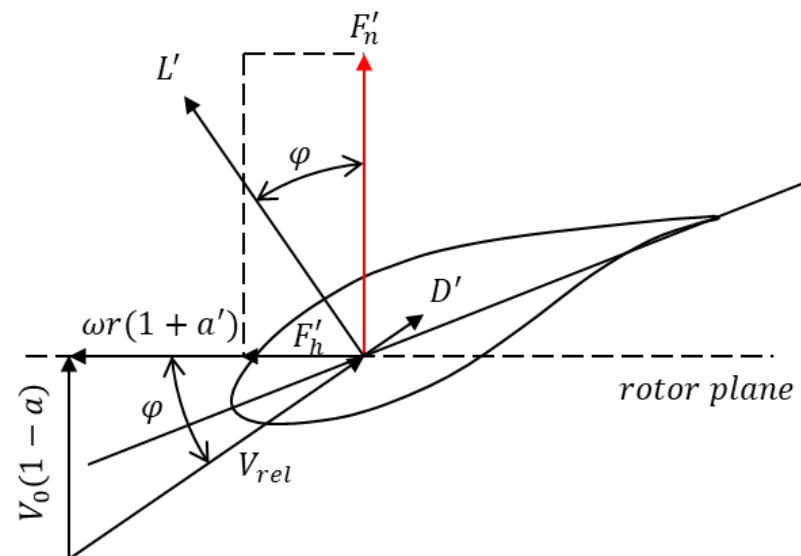


Figure 3. Aerodynamic loads in a blade section.

### 3. Blade Mass Modeling to Reduce Turbine LCoE

#### 3.1. LCoE of Wind Turbine

LCoE is expressed as an index that describes the economic feasibility of energy production and refers to the cost required to produce 1 kWh of energy. In wind turbine systems, LCoE is expressed as a function that incorporates initial installation and operating costs, as well as annual energy production, as shown in the following Equation [27]:

$$LCoE = \frac{CapEx \times FCR + OpEx}{AEP} \quad (4)$$

where CapEx is the initial capital costs of fixed assets, FCR is the fixed charge rate, and OpEx is cost during their operation. FCR accounts for financial factors such as the economic growth rate and depreciation across the period of wind turbine operation. According to the traditional scaling rule, the denominator in Equation (4) is proportional to the square of the blade radius, while the numerator is proportional to the cube of the blade radius (blade mass). This discrepancy can pose a challenge when attempting to reduce LCoE. Therefore, it is crucial to minimize the mass as the blades increase in size.

In this study, we focused on the blade material costs in determining CapEx because material costs accounted for 50–75% of the total cost of blades [20,24], as shown in Table 1. All other costs except for blade material assumed to be the same. In Section 4.2.2, we will compare the LCoE between turbines with the same AEP but different blade lengths. Assuming that the remaining variables in Equation (4) are identical, except for the blade cost, we can express the LCoE ratio between the turbines as follows [27]:

$$\beta = \frac{Cost_{blade} \times FCR}{CapEx \times FCR + OpEx} \quad (5)$$

$$\frac{LCoE}{LCoE_{ref}} = 1 - \left( 1 - \frac{Cost_{blade}}{Cost_{blade,ref}} \right) \beta \quad (6)$$

in which  $\beta$  expresses the fraction of the blade cost over the total cost of a wind turbine system. The subscript 'ref' in Equation (6) denotes a selected blade among those with different lengths. In this study, we will choose the blade that minimizes the LCoE.  $Cost_{blade}$  represents total cost of blade including materials, labor, tooling, and other related expenses [24]. The right-hand side of Equation (6) contains the relative proportion of the cost to the reference blade. While it is difficult to estimate the absolute cost of a blade, an increase or decrease in the relative cost to the reference blade is easy to express in a formula.

**Table 1.** Cost break-down for wind turbine blades.

Turbine/Project	Rated Power [MW]	Material [%]	Labor [%]	Etc. [%]
WindPACT [24]	1.5	47	26	27
IEA 3.4 MW [24]	3.4	48	25	27
SNL 100-00 [20]	13.2	72	14	14
SNL 100-01 [20]	13.2	75	12	13
SNL 100-03 [24]	13.2	60	16	24

### 3.2. Blade Mass Modeling

Material costs constitute the largest component of blade costs, followed by labor costs. Other expenses encompass overhead, capital, tooling, utility, and maintenance costs [24]. As the blade cost represents approximately 3–28% of the total turbine cost [1,11,21,28] as shown in Table 2, with material costs accounting for approximately 50–75% of the blade cost [20,24] as shown in Table 1, the contribution of blade materials to the overall turbine cost is estimated to be around 1.5–21%. The cost of blades typically accounts for around 10% of the total turbine cost. Additionally, implementing load reduction via the low-induction rotor concept and enhancing AEP through the low specific power design concept can decrease the LCoE associated with the turbine. We developed a blade mass ratio model for horizontal axis wind turbine to compare the LCoE of wind turbines with different blade numbers or axial induction factors. The cost of manufacturing, processing, and transporting each blade was not considered, only the cost of the material used to create each blade. To simplify the cost calculation process, first, each blade is divided into several blade elements of a certain length (Figure 4). Any blade element  $i$  and baseline blade element  $i_{base}$  that were compared were composed of the same materials at the same ratio. As blade elements were divided by the same length, the cost of each blade was calculated as the sum of the cost of each blade element. The ratio expressing the cost of a designed blade compared to the cost of the baseline blade was expressed as:

$$\frac{Cost_{blade}}{Cost_{blade,base}} = 1 + \alpha \left( \frac{Cost_{blade,material}}{Cost_{blade,material,base}} - 1 \right) \quad (7)$$

$$\frac{Mass_{blade}}{Mass_{blade,base}} = \frac{(cost\ per\ kg)\ (density)\ R\ \sum_1^i Area_i}{(cost\ per\ kg)\ (density)\ R_{base}\ \sum_1^i Area_{i,base}} \left( = \frac{Cost_{blade,mat}}{Cost_{blade,mat,base}} \right) \quad (8)$$

in which  $Area$  describe the blade sectional area of the blade element, and  $R$  denotes the tip radius of the rotor blade, respectively. The subscripts 'base' and 'mat' in Equations (7) and (8) denote a baseline turbine (NREL 5 MW reference wind turbine in this study) and material, respectively. Each blade mass ratio reflects blade length and the cross-sectional area of the material used at each blade element. Each blade element can be divided into skins, spars, and webs. In Equation (7),  $\alpha$  represents the percentage of material cost in the total cost of the blade and specifically ranges from 50% to 75% [20,24]. To focus on the blade mass only, we convert the blade cost ratio presented in Equation (7) to the blade mass ratio, as shown in Equation (8).

**Table 2.** Shares of the overall costs of various wind turbines.

Turbine/Project	Rated Power [MW]	Blades [%]	ICC [%]	O&M [%]	Etc [%]
Baseline of [1]	3	3.6	72.9	20.6	6.5
Ashur et al. [11]	20	28.4	87.9	3.9	8.4
Ashuri [21]	10	5.8	70.0	26.1	3.9
Ashuri [21]	20	8.2	73.5	23.2	3.3
INNWIND.EU [28]	10	3.73	62.5	37.5	-
INNWIND.EU [28]	10	3.78	61.6	38.4	-

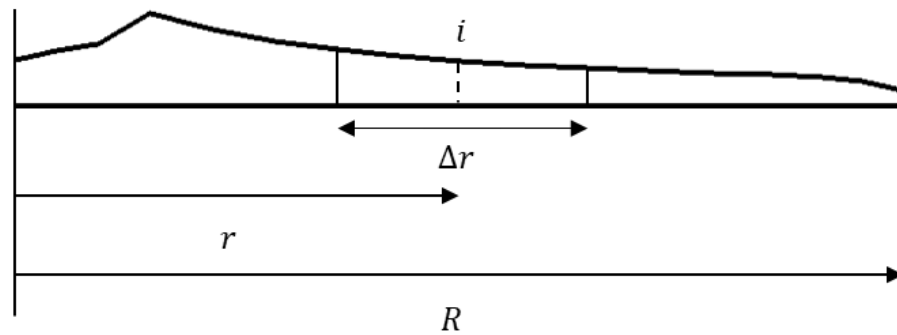


**Figure 4.** A blade element for the *i*th node.

As shown in Figure 5, skin was modeled simply as a hollow elliptical tube, while spars and webs were similarly modeled as a hollow rectangular tube. The hollow elliptical tube can be described in terms of chord length and airfoil thickness, which must be determined in order to perform an aerodynamic analysis of each blade, while skin thickness  $t_{skin}$  is an unknown variable. In our model blade section (Figure 5), the thickness of the spar and the thickness of the web were assumed to be identical ( $t_{spar} = t_{web}$ ). Web height, distance, and thickness were calculated as airfoil thickness ratio  $\tau$  multiplied by 0.9 [29], chord length multiplied by  $w$  (with  $w = 0.3$ ) [30], and skin thickness multiplied by  $\gamma$  ( $\gamma = 1.5$ ), respectively. Through these dimensional determinations, the cross-sectional area of the blade structure was expressed using Equation (9). The parameter  $f_A$  was then derived as a function of  $w$ ,  $\gamma$ , and  $\tau$  as shown in Equation (10). Ratios between airfoil thickness and chord length, i.e., airfoil thickness ratios, for all airfoils used for the wind turbine blade design are shown in the third column of Table 3.  $P_e/C$  in Table 3 expresses the perimeter length divided by the chord length.

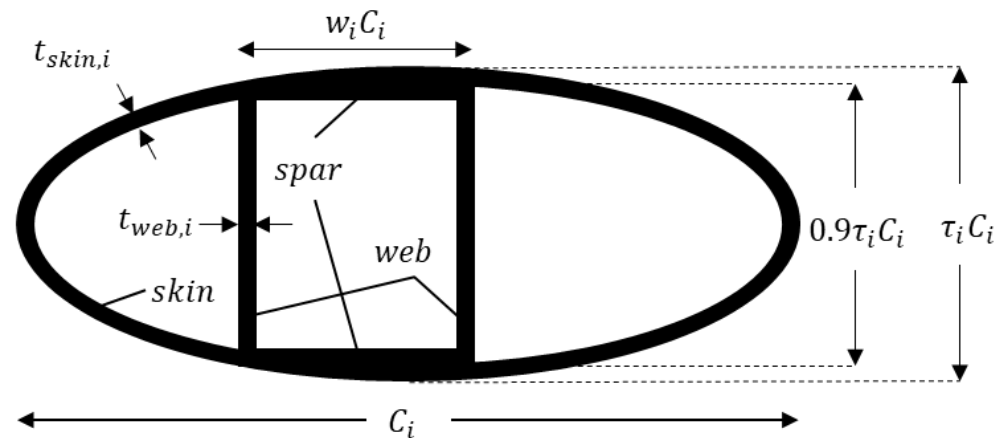


**Figure 5.** Structural modeling of a blade section for LCoE comparison.

**Table 3.** Airfoil distribution along each blade span.

r/R	Airfoil	Thickness Ratio	Perimeter Ratio of Airfoil ( $P_e/C$ )	Perimeter Ratio of Ellipse ( $P_e/C$ )	Relative Error [%]
0.046	Cylinder	1.00	6.28	6.28	0
0.089	Cylinder	1.00	6.28	6.28	0
0.132	Cylinder	1.00	6.28	6.28	0
0.187	DU99_W_405LM	0.40	2.28	2.39	4.8
0.252	DU99_350	0.35	2.22	2.35	5.9
0.317	DU99_350	0.35	2.22	2.35	5.9
0.382	DU97_W_300	0.30	2.16	2.32	7.4
0.447	DU97_W_300	0.30	2.16	2.32	7.4
0.512	DU97_W_300	0.30	2.16	2.32	7.4
0.577	DU91_W2_250	0.25	2.12	2.29	8.0
0.642	DU91_W2_250	0.25	2.12	2.29	8.0
0.707	DU91_W2_250	0.25	2.12	2.29	8.0
0.772	DU93_W_210LM	0.21	2.09	2.27	8.6
0.837	DU93_W_210LM	0.21	2.09	2.27	8.6
0.892	DU93_W_210LM	0.21	2.09	2.27	8.6
0.935	DU93_W_210LM	0.21	2.09	2.27	8.6
0.978	DU93_W_210LM	0.21	2.09	2.27	8.6

The mass ratio between the two blades can be expressed as a function of chord length and skin thickness, as shown in Equation (11). The right columns of Table 3 present the perimeter of an ellipse with the same thickness ratio as the corresponding airfoil perimeter, along with the relative error between the two values. The perimeter plays a crucial role in determining the mass and moment of inertia per unit length of the blade cross section. According to the results in Table 3, the relative error in the perimeter for both geometries is no more than 9%. Therefore, substituting the airfoil with an ellipse does not introduce a significant error. On the other hand, utilizing the ellipse simplification in the blade mass model offers the advantage of a highly concise expression, as shown in Equation (11).

$$Area_i = C_i t_{skin,i} f_A \quad (9)$$

$$f_A = \frac{\pi}{2} (1 + \tau_i) + 2\gamma (w_i + 0.9\tau_i) \quad (10)$$

$$\frac{Mass_{blade}}{Mass_{blade,base}} = \frac{R}{R_{ref}} \frac{B}{B_{ref}} \frac{\sum_1^i C_i t_{skin,i} f_A}{\sum_1^i C_{i,ref} t_{skin,i,base} f_{A,base}} \quad (11)$$

in which sectional parameters are presented in Figure 5.

Of the various loads acting on the rotor, we considered the flapwise bending moment at the blade root [31], which is directly affected by thrust acting on the rotor plane. Thus, we modelled the blade as a simple cantilever beam (Figure 6). We assumed that the bending stresses at the root of both the designed and the baseline blades were identical. Chord length and airfoil thickness at each blade section are known values, and the moment of inertia can be obtained using shape modeling (Figure 5). We assumed that each structural component—spar, skin, and web—resisted bending stress, similar to the wings of high-speed aircraft and very large wind turbine blades. Equation (16) was then obtained by rearranging Equations (12)–(15) into the equation of thickness:

$$\sigma = \sigma_{base} \quad (12)$$

$$\sigma = -\frac{M\tau_i C_i / 2}{I} \quad (13)$$

$$I_i = \frac{1}{8} \tau_i^2 C_i^3 t_{skin,i} f_I \quad (14)$$

$$f_I = \frac{\pi}{4} (3 + \tau_i) + \frac{27}{25} \gamma (3w_i + 0.9\tau_i) \quad (15)$$

$$t_{skin,i} = t_{skin,i,base} \frac{M}{M_{base}} \frac{\tau_{i,base} C_{i,base}^2 f_{I,base}}{\tau_i C_i^2 f_I} \quad (16)$$

in which  $I$  and  $M$  represent the area moment of inertia and flapwise bending moment at the root of the blade, while  $f_I$  denotes the coefficient of the area moment of inertia.

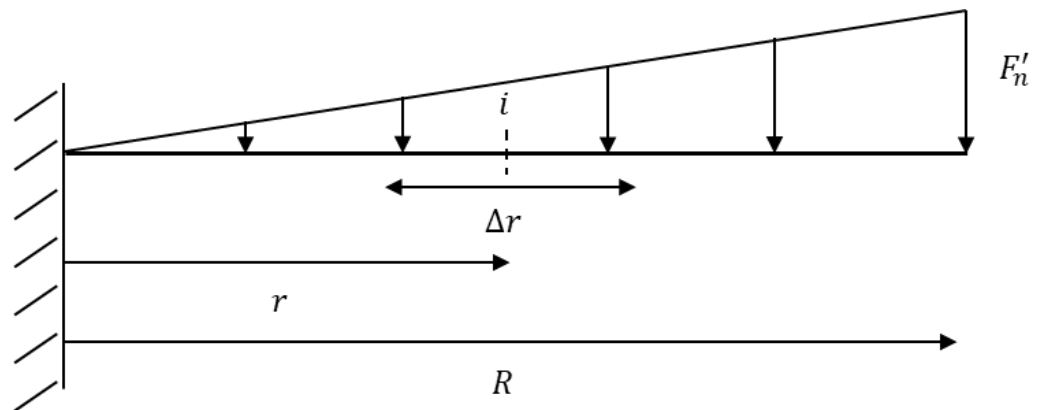


**Figure 6.** Load distribution along the blade span for LCoE comparison.

The flapwise bending moment at the blade root is caused by aerodynamic thrust, as confirmed through Equation (3). The flapwise bending moment along the blade span can be expressed through Equation (17), which incorporates our simplified cantilever beam assumption. The force acting on the cantilever beam can be expressed as a triangular distributed load along the spanwise direction (Figure 6).  $F'_n$  is the force per unit length acting on the end of the cantilever beam. Equation (19) can be obtained from Equations (11), (13), (17) and (18). Equation (19) shows that the ratio of the mass of the designed blade to the mass of the baseline blade (NREL 5 MW blade) is expressed as a function of airfoil thickness, chord length, axial induction, and blade length. According to the numerical simulation, the effects of the  $\gamma$  and  $w_i$  on the mass ratio determined through Equation (19) are negligible.

$$M = \frac{F'_n}{6R} (-2R^3 + 3R^2r - r^3) \quad (17)$$

$$F'_n = 4\rho\pi V_0^2 a(1-a)r/B \quad (18)$$

$$\frac{Mass_{blade}}{Mass_{blade,base}} = \frac{a(1-a)}{a_{ref}(1-a_{base})} \frac{R^4}{R_{base}^4} \frac{\sum_1^i C_{i,ref} t_{skin,i,base} f_A \frac{\tau_{i,base} C_{i,base} f_{I,base}}{\tau_i C_i f_I}}{\sum_1^i C_{i,base} t_{skin,i,base} f_{A,base}} \quad (19)$$

in which  $r$  shows the spanwise location of the blade element from the center of the rotor hub.

## 4. Results and Discussion

### 4.1. Considerations for Aerodynamic Rotor Design

#### 4.1.1. Aerodynamic Data of Airfoils

One of differences between the NREL 5 MW wind turbine and our 20 MW wind turbine is the distribution of airfoils along the blade. In particular, the NACA64-618 airfoil was not applied to the outboard section of our blades, as the longer blade length of the low-induction rotor required increased stiffness at the tip to prevent excessive twist or

deflection. Instead, we used a DU93\_W\_210LM airfoil at the outboard section of the blade, as shown in Table 3 [32,33].

To design a 20 MW class wind turbine rotor, the NREL 5 MW wind turbine was used as a baseline turbine, and the need for an increased Reynolds number consistent with an increase in blade chord length and rotational speed was considered for aerodynamic data correction. The Reynolds number of the 20 MW class wind turbine blade is approximately double (around  $Re = 20 \times 10^6$ ) that of the NREL 5 MW wind turbine. This value is high enough to influence aerodynamic performance, and lift and drag coefficients were revised to account for the airfoil's angle of attack at a high Reynolds number accordingly [33]. The results were used as the airfoil input data for the design of a 20 MW class low-induction rotor.

#### 4.1.2. Low-Specific Power Design

NREL 5 MW and DTU 10 MW reference wind turbines have some known shortcomings, including a too high specific power of  $401 \text{ W/m}^2$  (Table 4). In 2016, the IEA performed a survey to identify the use cases and need for reference wind turbines for research and development applications [4]. Nearly 58% of the respondents suggested a specific power lower than  $350 \text{ W/m}^2$ . The specific power of the IEA 15 MW reference wind turbine developed by NREL, DTU, and the University of Maine [4] was  $332 \text{ W/m}^2$ . Table 4 shows the specific powers of various reference wind turbines, including the NREL 5 MW, LEANWIND 8 MW [34], DTU 10 MW, AVATAR 10 MW [35], IEA 15 MW, ECN 20 MW, and INNWIND.EU 20 MW RWTs. Table 4 also presents relevant information concerning three commercial turbines: the GE Heliade-X 12 MW, and two Korean manufacturer's turbines. Notably, the two Korean system manufacturers plan to release wind turbines that reflect low specific power designs in accommodation of the wind conditions around the Korean Peninsula. Based on a wind resource assessment of measured wind data around the Korean Peninsula, the wind class around the sea areas of the Korean Peninsula at which fixed sub-structure type offshore wind turbines can be appropriately installed is 3 or more [36]. It follows that turbines with a lowered specific power design are suitable for the West Sea area of the Korean Peninsula. Fundamentally, the low-induction rotor is attractive in low wind speed areas because it has the property of producing a lower specific power, which makes it more efficient in such conditions.

**Table 4.** Powers for reference turbines and selected commercial turbines.

Turbine/Project	Rated Power [MW]	Rated Wind Speed [m/s]	Rotor Diameter [m]	Specific Power [ $\text{W/m}^2$ ]
NREL 5 MW [2]	5	11.4	126	401
DTU 10 MW [5]	10	11.4	178.3	401
IEA 15 MW [4]	15	10.59	240	332
ECN 20 MW [10]	20	10.0	252	401
INNWIND.EU 20 MW [17]	20	11.4	252	401
LEANWIND [34]	8	12.5	164	379
AVATAR [35]	10	10.4	205.8	300
GE 12 MW	12		220	316
Unison 10 MW	10	12.0	209	292
Doosan 8 MW	8	10.5	205	242

#### 4.1.3. Basic Design Parameters for 20 MW Wind Turbine

PROPID [37] is a wind turbine aerodynamic design tool that allows for an inverse design process in which desired variables, such as axial induction factor or lift coefficient along the blade span, are inputted first. Therefore, using this software, unlike an optimal aerodynamic design in which an axial induction factor is set to  $a = 1/3$ , a user can set the desired axial induction factor to obtain an appropriate blade geometry. We set axial

induction factor values at  $a = 0.2 \sim 0.3$  for our low-induction rotor, and the value of the axial induction factor was set to be constant at each blade section (except for the inboard cylinder part of the blade). The basic parameters of our low-induction rotor for use in a 20 MW class wind turbine are shown in Table 5.

**Table 5.** Basic design parameters for low-induction rotors.

Descriptions	Values
Rated power [MW]	20
Number of blades	3
Blade length [m]	150.81~162.55
Rated wind speed [m/s]	10
Tip speed ratio [-]	9
Rated rotational speed [rpm]	5.54~5.7
$C_{p,max}$ [-]	0.421~0.489
Axial induction factor $a$	0.2~0.3

The aerodynamic design process for our 20 MW RWT proceeded with a rated wind speed of 10 m/s. The tip speed ratio of the NREL 5 MW wind turbine is 7, while that of our 20 MW wind turbine is as high as 9. As the 20 MW wind turbine is sufficiently far from the seashore, concerns over noise impacts are not acute, and aerodynamic performance can be improved by increasing the rotational speed (or Reynolds number).

Additional aerodynamic analysis of a rotor for a 20 MW wind turbine was performed using FAST software to examine the aerodynamic design of the blade [3]. Prior to this study, the results of the aerodynamic analyses of two tools, PROPID and FAST, had been cross-validated [38], and we likewise obtained the same numerical results of the  $C_p - \lambda$  curves (Figure 7) of an aerodynamically optimized blade for a 20 MW wind turbine rotor.

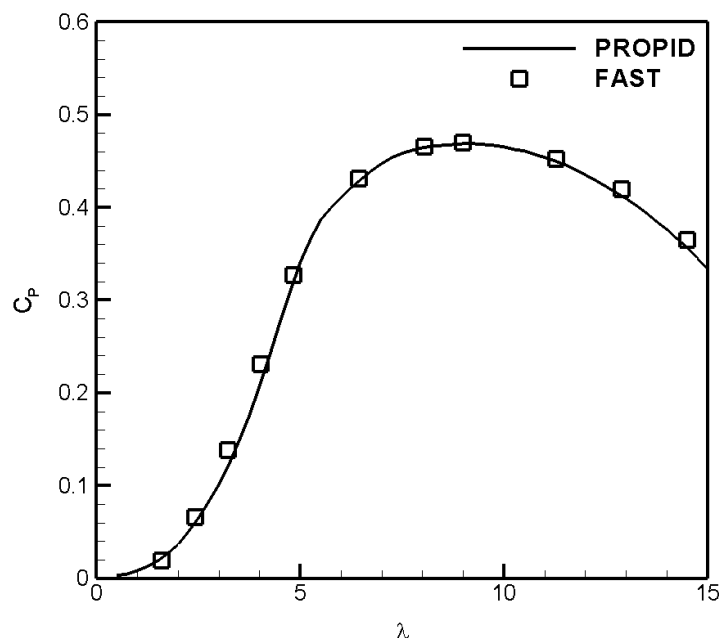


**Figure 7.**  $C_p - \lambda$  curve of a test rotor compared using PROPID and FAST.

## 4.2. Low LCoE Design for 20 MW Wind Turbine Rotor

### 4.2.1. Validation of Mass Model

To compare the blade mass using Equation (19), blade skin thickness had to be determined. However, since the skin thickness of the 20 MW class low-induction rotor is

unknown, Equation (19) was used to express the ratio of blade mass. In this manner, the mass of each low-induction rotor could be simultaneously compared. In other words, although the absolute mass of each blade was unknown, the relative mass of each was expressed by Equation (20). We assumed that the web distance  $w$  and the ratio  $\gamma$  of the skin of the corresponding blade element of the 20 MW class low-induction blade had the same value as the NREL 5 MW wind turbine blade. It is assumed that the normalized positions of the airfoils used in the blades targeted in this study are the same.

$$\frac{Mass_{blade}}{Mass_{blade,case1}} = \frac{a(1-a)R^4 \sum C_{i,5MW} t_{skin,i,5MW} f_A \frac{\tau_{i,5MW} C_{i,5MW} f_{l,i,5MW}}{\tau_i C_i f_{l,i}}}{a_{case1}(1-a_{case1})R_{case1}^4 \sum C_{i,5MW} t_{skin,i,5MW} f_{A,case1} \frac{\tau_{i,5MW} C_{i,5MW} f_{l,i,5MW}}{\tau_{i,case1} C_{i,case1} f_{l,i,case1}}} \quad (20)$$

In Equation (20), the subscripts “Case 1” and “5 MW” denote the values of the blade parameters for Case 1 and the NREL 5 MW blade [2], respectively. These values are used to estimate the mass distribution of the wind turbine blade using the mass model presented in this study.

By utilizing Equation (9), the mass at each node ‘ $i$ ’ of the wind turbine blade can be expressed as Equation (21). Furthermore, Equation (21) can be transformed into Equation (22) through the use of Equations (16)–(18). This allows for the estimation of the mass at each node ‘ $i$ ’ of an arbitrary wind turbine blade, leveraging the known information from the NREL 5 MW of wind turbine blades (baseline blades).

$$Mass_{blade,i} = C_i t_{skin,i} f_{A,i} \Delta R_i (density_i) \quad (21)$$

$$Mass_{blade,i} = C_{i,5MW} t_{skin,i,5MW} f_{A,i} \Delta R_i (density_{i,5MW}) \frac{a(1-a)R^4}{a_{5MW}(1-a_{5MW})R_{5MW}^4} \frac{\tau_{i,5MW} C_{i,5MW} f_{l,i,5MW}}{\tau_i C_i f_{l,i}} \quad (22)$$

To validate Equation (22), we used two wind turbine rotors proposed by different sources: a 3.4 MW rotor proposed by the IEA [39] and a 10 MW reference rotor proposed by DTU [5]. We estimated the mass distributions of both blades using the mass model, scaling rule and compared the results, as shown in Figures 8 and 9. The simple scaling rule shows the largest error with the blade mass distribution. Based on the comparison results, we can conclude that the mass distribution modeling used in this study is reliable. The blade masses for several reference wind turbines and the masses calculated using Equation (22) are presented in Table 6. It is evident that the presence or absence of MDAO has an impact on the difference between the two blade masses. Most of the blades that underwent MDAO are lighter compared with the masses obtained using Equation (22) for those that did not. In particular, the SNL 100-03 blade, which is derived from the SNL 100-00 blade and utilizes lighter materials through stepwise optimization, exhibits a significant improvement in mass reduction.

**Table 6.** Comparison of the mass predicted by the mass model for the reference wind turbines.

Turbine	MDAO	Rated Power [MW]	Blade Radius [m]	Blade Mass [kg]	Predicted Mass [kg]
NREL 5 MW [2]	X	5	63	17,740	17,740
IEA 15 MW [4]	O	15	120	65,250	189,169
DTU 10 MW [5]	O	10	89.15	41,722	47,172
ECN 20 MW [10]	X	20	123	161,000	135,383
Ashuri 20 MW [11]	O	20	135	259,000	215,072
SNL 100-03 [13]	X	13.2	100	49,519	101,232
IEA 3.4 MW [39]	O	3.4	65	16,441	22,147
SNL 100-00 [40]	X	13.2	102.5	114,172	80,581

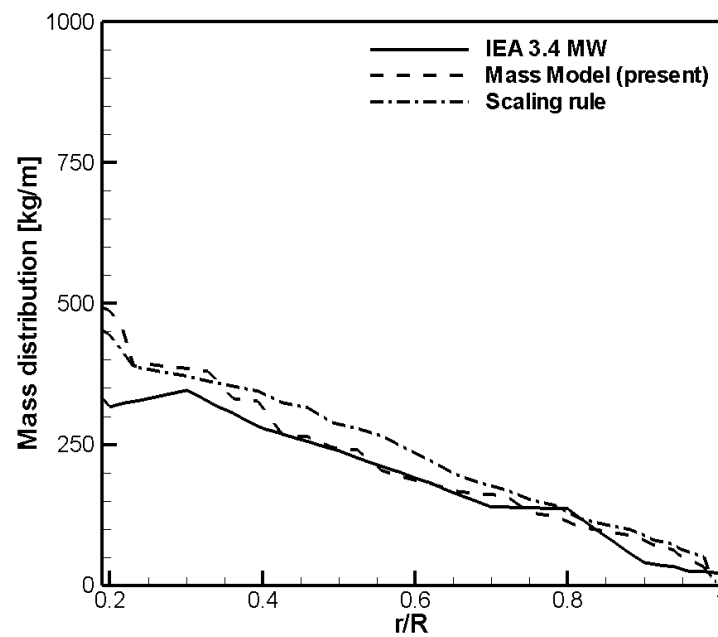


Figure 8. Comparison of spanwise mass distribution for the IEA 3.4 MW [39] wind turbine.

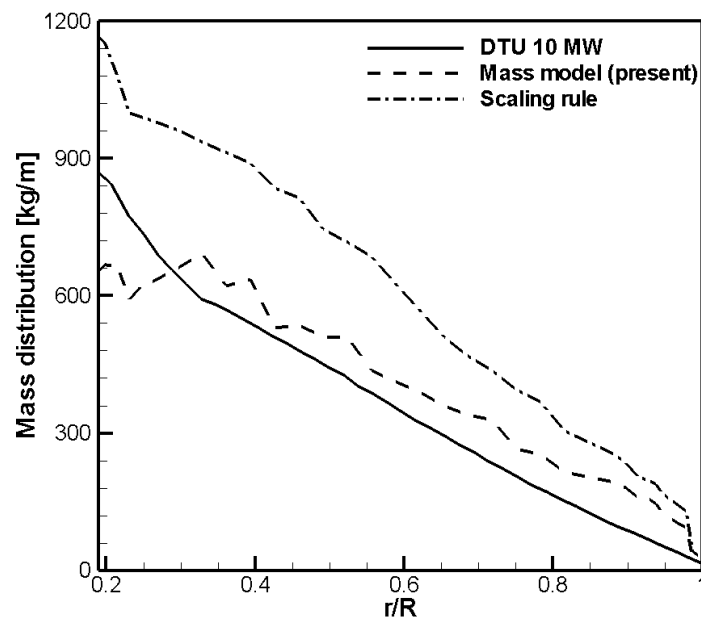
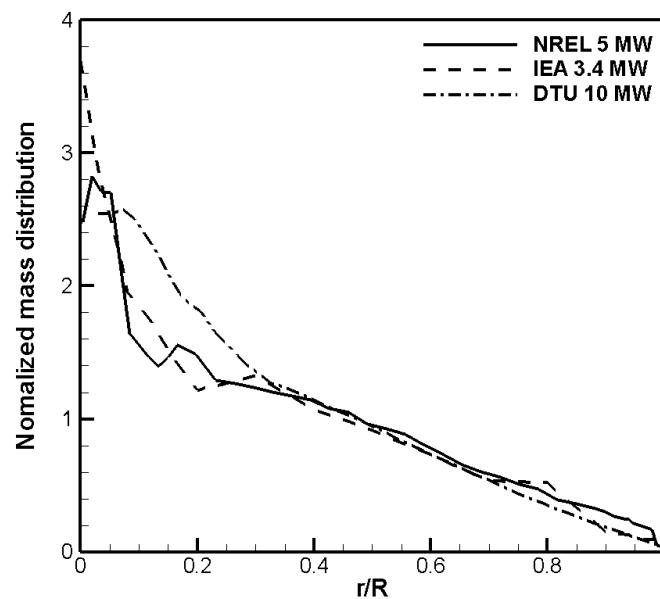


Figure 9. Comparison of spanwise mass distribution for the DTU 10 MW [5] wind turbine.

Figure 10 illustrates the non-dimensional mass distribution of the NREL 5 MW, IEA 3.4 MW, and DTU 10 MW wind turbine blades. The length and mass of each blade element are non-dimensionalized by the blade radius and blade mass, respectively. The outboard section of the blades exhibits good agreement, while discrepancies arise in the inboard section. These differences suggest variations in material density within the inboard blade elements or differences in the non-dimensional dimensions of structures such as the skin, spar, and web (see the dimensions of the structure of Figure 5 in Section 3.2). These disparities can manifest during the MDAO process, leading to observable variations in the mass distribution, particularly in the inboard part of the blade, as shown in Figures 8 and 9.



**Figure 10.** Comparison of spanwise normalized mass distribution for three selected reference wind turbines.

#### 4.2.2. Axial Induction Factor for Lowest LCoE

Two low-induction rotors were selected as comparators to confirm the difference according to the reference for comparison. The aerodynamically optimal 20 MW rotor with  $a = 0.3$  is referred to as Case 1, which is close to  $a = 1/3$ . The first low-induction rotor with  $a = 0.2$  is referred to as Case 2. The blade corresponding to the lowest mass is named Case 3. The specifications for these blades are shown in Table 7. If the value of the axial induction factor corresponding to the lowest value of the blade mass ratio changes depending on the value of the denominator in the left-hand-side term of Equation (20), it would suggest that there is a problem in determining the axial induction factor with the lowest blade mass model. To confirm this, the variation of the blade mass ratios according to the axial induction factor was determined as the denominator of Equation (20) was changed to corresponding blade mass of Case 1 and Case 2 rotors. The results confirmed that there were no problems in determining the lowest mass axial induction factor as shown in Figure 10. Notably, the blade mass was lowest at  $a = 0.26$ .

**Table 7.** Specifications of designed 20 MW rotors.

Descriptions	Case 1 Rotor	Case 2 Rotor	Case 3 Rotor
Number of blades		3	
Blade length [m]	150.81	162.55	154.02
Blade length/Blade length_Case 1 [%]	100	107.8	102.1
Cut-in wind speed [m/s]		3	
Rated wind speed [m/s]		10	
Cut-out wind speed [m/s]		25	
Tip speed ratio [-]		9	
Rated rotational speed [rpm]	5.7	5.29	5.58
$C_{p,max}$ [-]	0.4888	0.4207	0.4686
$C_{p,max}/C_{p,max\_Case 1}$ [%]	100	86.1	95.9
Designed axial induction factor $a$ [-]	0.3	0.2	0.26
Blade mass/Blade mass_Case 1 [%]	100	102.2	92.0

We then checked whether the change of  $\beta$  in Equation (5) affected the selection of the axial induction factor corresponding to the lowest LCoE. The range of the  $\beta$  generally being

between 3% and 27% [1,11,21,28], the LCoE ratio of the low-induction rotor was compared for  $\beta = 0.05, 0.1, 0.15$  and  $0.2$  as shown Figure 11. As we already saw in Figure 12, the axial induction coefficient for the lowest LCoE was still 0.26, as shown in Figure 11, suggesting that variations in  $\beta$  also did not affect the determination of which low-induction rotor resulted in the lowest LCoE. Accordingly, Case 3 includes the rotor with the lowest LCoE, as designed by an axial induction factor of 0.26. The mass of the Case 3 rotor is 8% less than the Case 1 rotor based on Figure 12 and Table 7.

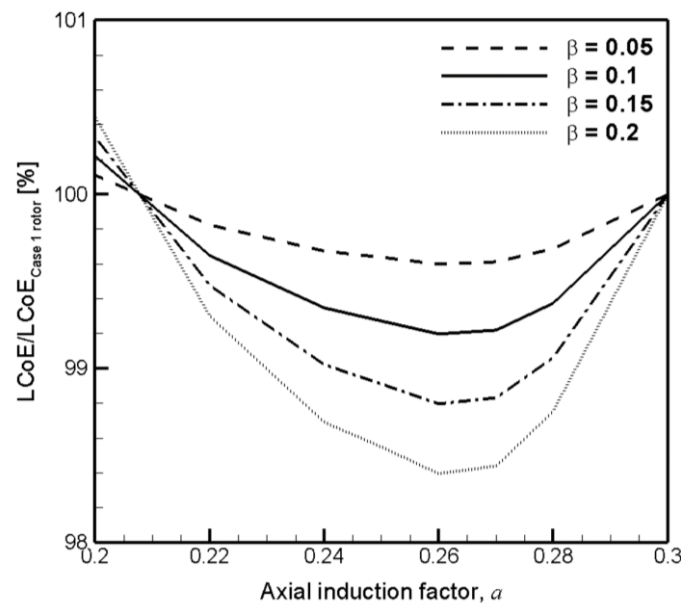


Figure 11. Normalized LCoE for various  $\beta$  values.

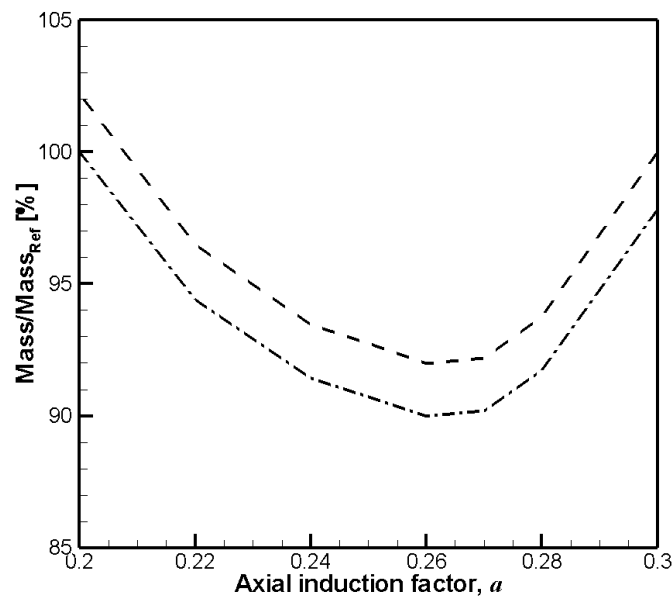


Figure 12. Mass ratio of Case 1 and Case 2 according to axial induction factor.

Table 8 presents a comparison of the LCoE results for the 20 MW wind turbine studied by Ashuri et al. [11] and the Case 1, Case 2, and Case 3 rotors in this study. The mass and cost models employed in this study utilize the scaling rule to estimate the mass and cost of individual wind turbine components. Specifically, the blade mass and cost model can be

expressed as Equations (23) and (24), while the tower mass and cost model can be described by Equations (25) and (26) [1,21].

$$Mass_{blade} = 0.1452 \times R^{2.9158} \quad (23)$$

$$Cost_{blade} = (13.084 \times Mass_{blade} - 4452.2) \times (1 + PPI) \quad (24)$$

$$Mass_{tower} = 0.697 \times (swept\ area) \times (hub\ height) - 1414 \quad (25)$$

$$Cost_{tower} = 1.5 \times Mass_{tower} \times (1 + PPI) \quad (26)$$

**Table 8.** Comparison of LCoE calculation results for a 20 MW wind turbine [11].

Equipment	Ashuri 20 MW [11]		Case 1		Case 2		Case 3	
	Cost [k\$]	Mass [ton]	Cost [k\$]	Mass [ton]	Cost [k\$]	Mass [ton]	Cost [k\$]	Mass [ton]
Blade	4051.7	259	3735.8	228.4	3831.4	234.2	3430	209.7
Hub	1456.9	252.8	1288.4	223.6	1320.5	229.1	1185.8	205.8
Pitch system	1945.3	236	2468.6	208.3	3005.6	213.5	2604.3	191.4
Hub cone	34.6	4.6	38.2	5.1	41.5	5.5	39.1	5.2
Main shaft	1605.3	159.1	2073.6	205.6	2575	255.3	2203.7	218.5
Shaft bearing	1013.4	42.5	1380.2	57.8	1795.4	75.2	1486	62.3
Gearbox	4955.5	161.9	4981.9		4981.9		4981.9	
Drive train brake	44.4	4	44.6	4	44.6	4	44.6	4
Generator	1592.2	59.8	1599	60	1599	60	1599	60
Electronics	1572.8		1572.8		1572.8		1572.8	
Yaw system	1495	176.8	1945	237.3	2429.1	304.2	2070.3	254.5
Nacelle frame	752.6	280.8	895.1	348.6	1036.3	403.6	932.7	363.2
Nacelle railing	414.2	35.1	514.1	43.6	595.1	50.4	535.6	45.4
Nacelle cover	279.6	23.4	291.8	23.5	291.8	23.5	291.8	23.5
Turbine connection	1235.5		1247.2		1247.2		1247.2	
Cooling and hydraulic system	309	1.6	310.3	1.6	310.3	1.6	310.3	1.6
Monitoring and safety system	65.4		65.4		65.4		65.4	
Tower	3971	1588.3	3971.0	1588.3	3971.0	1588.3	3971.0	1588.3
Turbine Capital Costs	34,897.8		35,888.5		38,376.6			
Foundation	290.7		290.7		290.7		290.7	
Installation	363.1		363.1		363.1		363.1	
Farm connection	838.2		838.2		838.2		838.2	
Site assessment and permit	934.5		934.5		934.5		934.5	
Balance of Station	2426.5		2426.5		2426.5		2426.5	
Initial Capital Cost	37,324.3		38,315		40,803.1		37,858	
Levelized Replacement Cost	249.3		249.3		249.3		249.3	
Maintenance and Operation	108.7		118.1		118.1		118.1	
Interest Rate (FCR)	0.07		0.07		0.07		0.07	
AEP [GWh]	86		93.4		93.4		93.4	
LCoE [\$/kWh]	0.03454	(0.03051)	0.03263	(0.02890)	0.03450	(0.03077)	0.03229	(0.02856)

The PPI in Equations (24) and (26) is an index that is updated on a monthly basis to track the changes of costs of products and materials over a wide range of industries and industrial products [21].

To calculate the LCoE in Table 8, we use the blade masses of Case 1, Case 2, and Case 3 calculated by the mass model in this study. We can calculate the cost of pitch system, hub cone, main shaft, shaft bearing, yaw system, nacelle frame, nacelle railing as a function of blade length, and the cost of Gearbox, Electronics, Nacelle cover, turbine connection, cooling and the hydraulics system, Monitoring and safety system as a function of wind turbine rotor rated power. With the aforementioned assumptions, it is assumed that BOS (Balance of Station), LRC (Levelized Replacement Cost), M&O (Maintenance and Operation), IR (Interest Rate, FCR) are equal [11]. For AEP estimation in Case 1, Case 2, and Case 3, we employ the Weibull distribution with coefficients  $c = 9.47$  and  $k = 2$ . Comparing the LCoE of the wind turbine system with the Case 1, Case 2, and Case 3 rotors, we observed that the Case 3 rotor shows a decrease in LCoE of approximately 1% compared to the Case 1 rotor, 6.8% compared to the Case 2, and 7% compared to the Ashuri et al. 20 MW rotor. In addition, the LCoE value in parentheses bottom of Table 8 is the LCoE when considering a wind turbine without a gearbox, and the Case 3 rotor has an LCoE reduction of about 1.2% compared with the Case 1 rotor, about 7.8% compared with the Case 2 rotor, and about 6.8% compared with the Ahuri et al. 20 MW rotor. Based on these results, it is confirmed that the Case 3 rotor, obtained by applying the mass model proposed in this study, achieves the lowest LCoE.

#### 4.2.3. Case Study for Different Rotor Design

Figure 13 shows the power coefficient curves according to the tip speed ratio for various low-induction factors in cases in which  $a = 0.2$  (Case 2 rotor in Table 7), 0.26 (Case 3 rotor in Table 7), and 0.3 (Case 1 rotor in Table 7), and confirms that the design axial induction factor affects the power coefficient curve. The axial induction factor  $a = 0.2$  was chosen to maximize the objective function of  $C_P/C_M^{2/3}$  without losses, based on the study by Chaviaropoulos and Sieros [41]. The maximum value of the power coefficient of the Case 3 rotor is 4.1% smaller than the Case 1 rotor shown in Table 7. The reduction has a direct impact on annual energy production (AEP). Recalling from Equation (27) that the square of the rotor length and the power coefficient are inversely proportional, to equalize all AEPs for the low-induction rotors, the blade length of each low-induction rotor was adjusted to match Figure 14 or the power curve. The adjusted blade lengths were also applied to the blade mass ratio model shown in Equation (19).

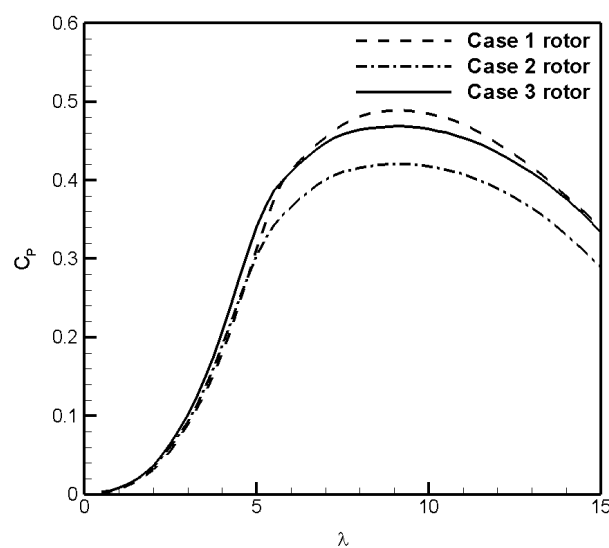


Figure 13.  $C_p - \lambda$  curves for various axial induction factors.

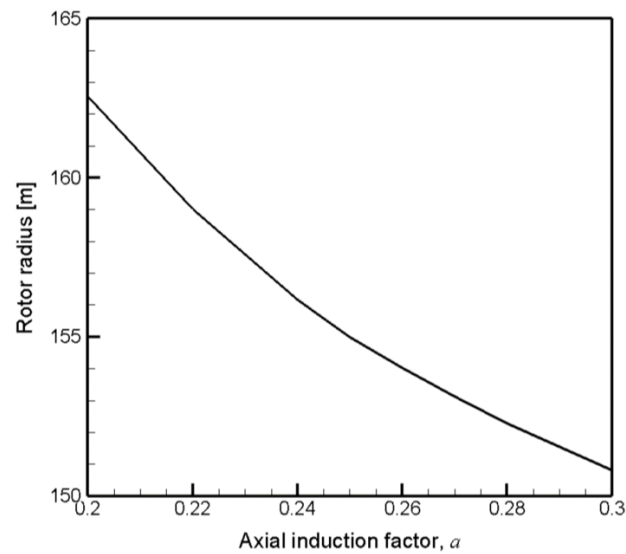


Figure 14. Rotor radius to compensate for  $C_{p,max}$  reduction.

$$P = C_p \frac{1}{2} \rho A V_0^3 \quad (27)$$

All blades were designed based on identical power curve assumptions. The power curves for Case 1, Case 2, and Case 3 rotors, as determined through PROPID, are shown in Figure 15 and all curves were confirmed to match well with each other. In this study, the 20 MW reference wind turbine model is a direct-drive type without a gear box, and the rated power, accounting for both the efficiencies of the generator and the power converter, is 21.4 MW at a rated wind speed of 10 m/s. This reflects a mechanical transmission efficiency of 99%, a generator efficiency of 96%, and a power conversion efficiency of 98.5% [32].

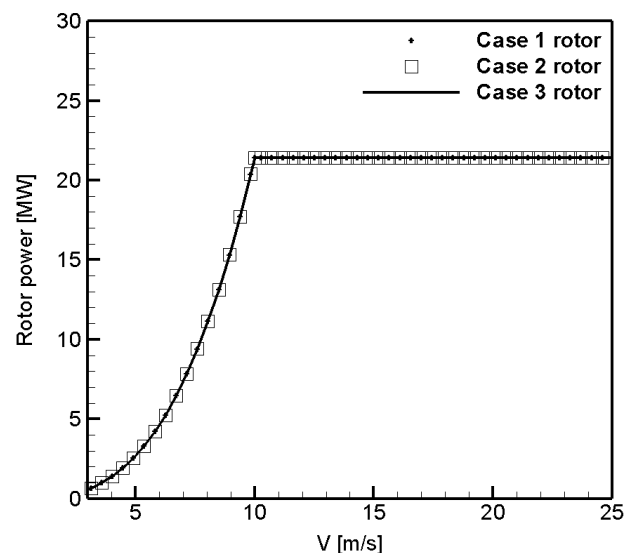


Figure 15. P-V curve for Case 1, Case 2, and Case 3 rotors.

The shapes and specifications of the Case 1, Case 2, and Case 3 blades are shown in Figures 16 and 17, and Table 7, respectively. Comparing each Case, we note that a decrease in the axial induction factor correlates with an increase in the twist angle (Figure 17). However, the Case 3 blade has the longest chord length among the low-induction rotors (Figure 16). Figure 18 highlights that the low-induction rotors, including Case 2 and Case 3, had a lower flapwise bending moment at the blade root than the Case 1 rotor. In particular, variation of the bending moment according to the wind speed at the blade roots for the Case

3 rotor which has both  $a = 0.26$  and the lowest LCoE are not significantly different compared to the loads generated by the Case 1 rotor with  $a = 0.2$ . This means that the low-induction rotor design with a slightly higher axial induction factor does not compromise the structural integrity of the blade and can still meet the load requirements. This is beneficial because it allows for a reduction in the amount of material needed to reinforce the blade, which can lead to lower costs and a more efficient design. Finally, the mass distributions along the blade span of the Case 1, Case 2, and Case 3 blades are shown in Figure 19.

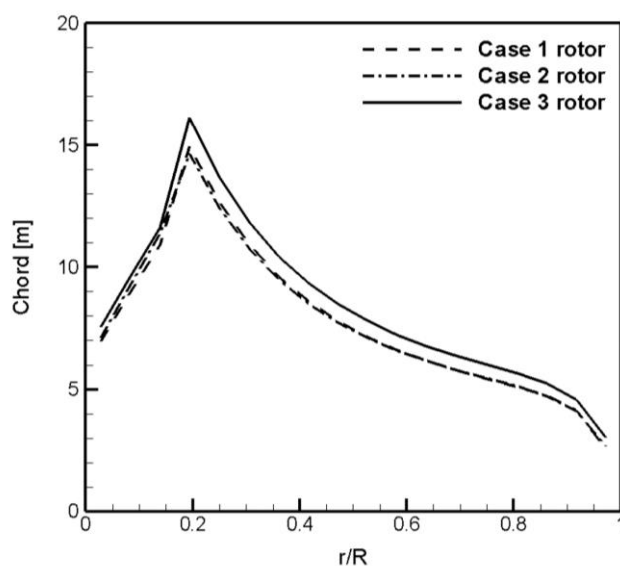


Figure 16. Chord length along the blade span for Case 1, Case 2, and Case 3 rotors.

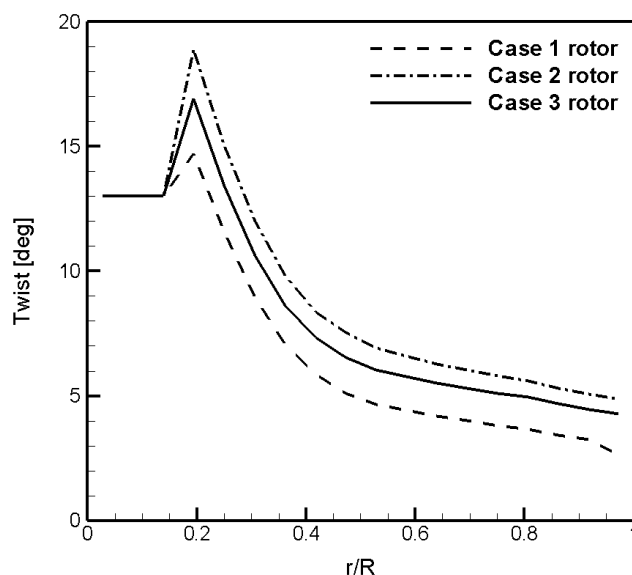


Figure 17. Twist angle along the blade span for Case 1, Case 2, and Case 3 rotors.

Figure 20 shows that the normalized LCoE ratio of the aerodynamically optimized two-bladed rotor is lower than that of the aerodynamically optimized three-bladed rotor (Case 1), at least when the rated wind speed and tip speed ratio for the rotors are the same (Table 5). Figure 21 highlights that the total mass of the two-bladed wind turbine rotor with the lowest LCoE is 27% less than that of the three-bladed Case 1 rotor. Considering that the ratio of blades to total wind turbine price is 0.1, a 27% decrease in blade cost corresponds to a 2.7% decrease in LCoE. However, the maximum value of the power coefficient for two-bladed rotor with the lowest LCoE is 0.4563 as shown in Figure 21; thus, the maximum

value of the power coefficient for the two-bladed rotor is 2.6% less than that of the three-bladed rotor with the lowest LCoE (Case 3). As a general matter, the two-bladed rotor, when compared to its three-bladed counterpart, does not have enough margin to avoid resonance between the tower frequency and the blade passage frequency [42]. The two-bladed rotor also experiences a larger tip loss effect, and would require a teetering hinge at the hub to reduce the loads due to the noted aerodynamic unbalance [42]. Moreover, the mass moment of inertia of the wind turbine rotor for the yawing axis is a function of the azimuth angle of the blade. We note that the operation of the two-bladed wind turbine rotor generates moment fluctuation during yawing motion. For these reasons, this study adopted the three-bladed rotor as the default RWT. Blade cost can be reduced to 8% less than that of the aerodynamically optimized blade.

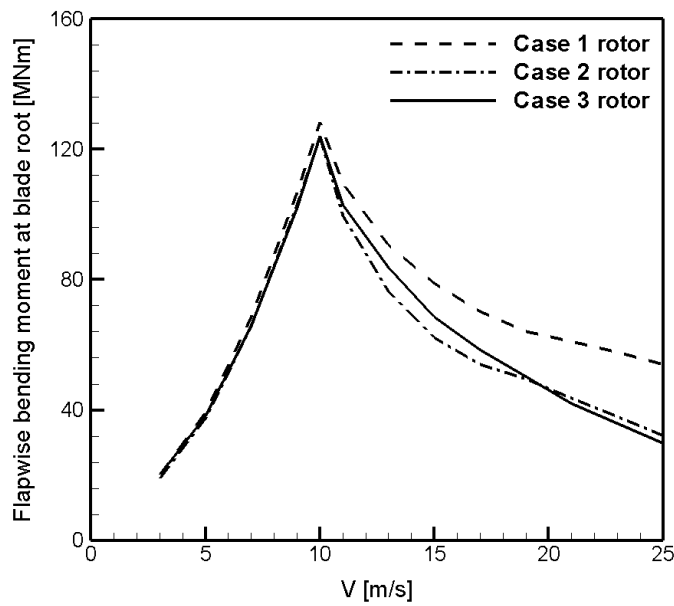


Figure 18. Load-V curve for Case 1, Case 2, and Case 3 rotors.

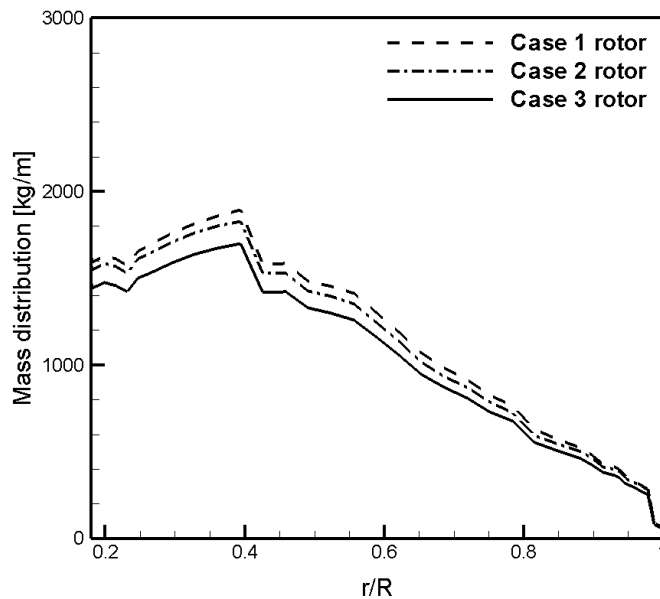


Figure 19. Mass per unit length along the blade span for Case 1, Case 2, and Case 3 rotors using Equation (22).

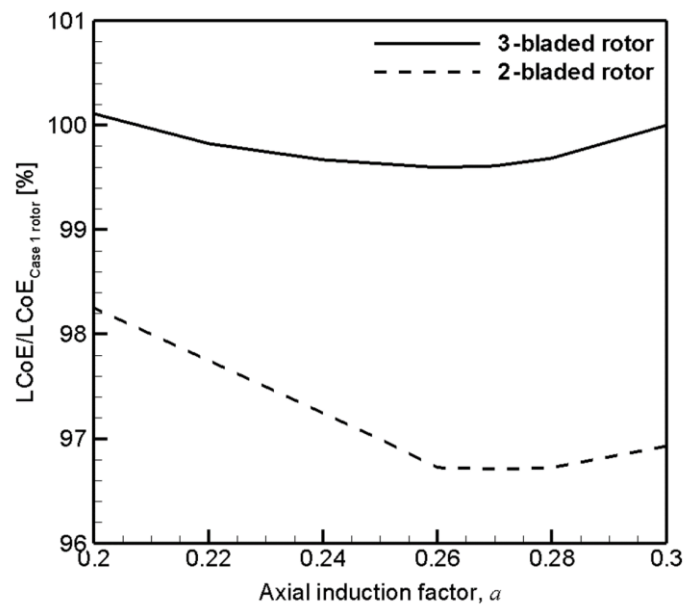


Figure 20. Normalized LCoE ratio of the two-bladed and three-bladed rotor.

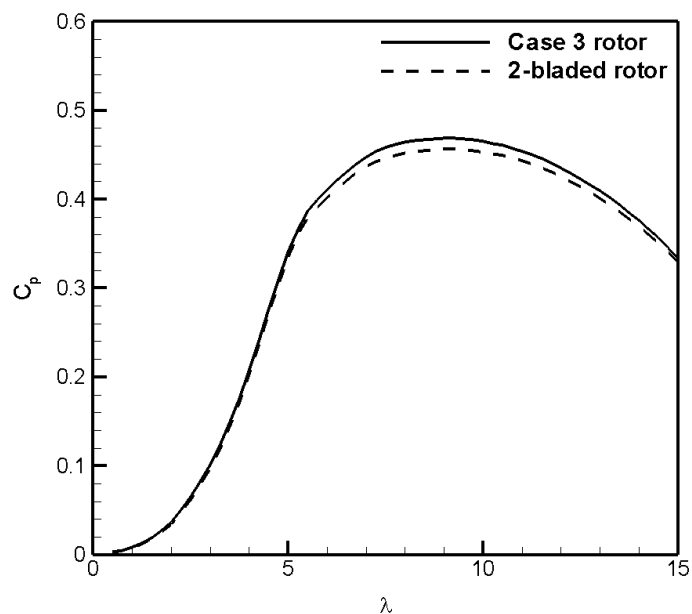


Figure 21.  $C_p - \lambda$  curves for Case 3 and a two-bladed rotor.

## 5. Conclusions

We developed a blade mass model and implemented it in the design of a 20 MW offshore rotor, utilizing a low-induction and low-specific power approach. The primary objectives of this design effort are to decrease the aerodynamic load on the blades through the low-induction concept, enhance the annual energy production (AEP) through the low-specific power concept, reduce blade costs, and ultimately achieve a lower levelized cost of energy (LCoE) for the wind turbine. A mathematical formula to express the mass ratio, which is the function of the axial induction factor,  $a$ , and blade shape, was also presented. All of airfoils' aerodynamic data were calibrated to fit the Reynolds number of the 20 MW wind turbine blade.

The mass ratio formula showed that the lowest LCoE for the 20 MW wind turbine was achievable at  $a = 0.26$ , and this result was consistent when the blade's share of the total system price was changed. Both the blade geometry along the spanwise direction and the

power coefficient  $C_p$  according to the tip-speed-ratio  $\lambda$  of three selected axial induction factors ( $a = 0.2, 0.26, 0.3$ ) were compared using PROPID's reverse design process. We confirmed that the bending moment of the low-induction rotor ( $a = 0.26$ ) at the blade root was less than that of the aerodynamically optimized rotor ( $a = 0.3$ ). However, the maximum power coefficient value of the low-induction rotor was 4.1% less than that of the optimized rotor. This reduced performance was compensated for by increasing blade length to satisfy the same power curve assumptions. Overall, the low-induction rotor at  $a = 0.26$  achieved an 8% reduction in mass compared to the aerodynamically optimized rotor at  $a = 0.3$ . By evaluating the LCoE parameters of each turbine component, the LCoE of the three 20 MW turbines developed in this study was calculated and compared to the LCoE of another wind turbine of the same capacity. The results showed that the LCoE of the low-induction rotor turbine (Case 3) not only had the lowest value, but it was also 7% smaller than the LCoE of the fourth wind turbine used for comparison.

Although a two-bladed rotor reduces costs by 27% more than a three-bladed rotor, we selected a three-bladed rotor for the 20 MW reference wind turbine. This decision was made because the two-bladed rotor experiences a reduced resonance avoidance margin with the tower, moment fluctuations during yawing motion, a diminished maximum power coefficient, and requires a teetering hub.

Finally, distribution of mass per unit length along the blade span was presented for the three-bladed upwind type rotor, reflecting the airfoil types, blade geometry, and shapes of internal structures such as spars and webs. The devised blade mass ratio model has shown itself to be a suitable formula for the preliminary design of blade shapes and estimation of mass distribution along the blade span for use in ultra-large scale reference wind turbines. The mass model of the blade proposed in this study can be utilized to obtain blade data, including mass and stiffness distribution along the blade span. This blade data is valuable for conducting comprehensive analyses using aeroelastic tools. Unlike the mass distribution result obtained through a simple scaling rule, this blade data reflects the concept of reducing the LCoE of the wind turbine.

**Author Contributions:** Conceptualization, K.-H.J. and K.-W.R.; methodology, K.-H.J. and K.-W.R.; software, K.-H.J.; validation, K.-W.R.; formal analysis K.-H.J. and K.-W.R.; investigation, K.-H.J. and K.-W.R.; resources, K.-H.J. and K.-W.R.; data curation, K.-H.J. and K.-W.R.; writing—original draft preparation, K.-H.J.; writing—review and editing, K.-W.R.; visualization, K.-H.J. and K.-W.R.; supervision, K.-W.R.; project administration, K.-W.R.; funding acquisition, K.-W.R. All authors have read and agreed to the published version of the manuscript.

**Funding:** This research was funded by Korea Electric Power Corporation, grant number R21XO01-6 and supported by Research Base Construction Fund Support Program funded by Jeonbuk National University in 2021.

**Data Availability Statement:** Not applicable.

**Conflicts of Interest:** The authors declare no conflict of interest.

## Nomenclature

$a$	Axial induction factor
$a'$	Tangential induction factor
$B$	Number of blades
$C_i$	Chord length at the $i$ th blade element
$C_p$	Power coefficient
$C_T$	Thrust coefficient
$F'_n$	Normal aerodynamic force at a rotor plane
$I$	Area moment of inertia
LCoE	Levelized cost of energy
$M$	Bending moment at radial position $r$
$r$	Radial position from rotating axis

$R$	Rotor radius
$t$	Thickness of airfoil skin, spar, and web
$u$	Wind speed at rotor plane
$V_0$	Free stream wind speed
$V_{rel}$	Effective wind speed
$w$	Distance between webs
$\alpha$	Ratio of a blade material cost to the total blade cost of a wind turbine system
$\beta$	Ratio of a blade cost to the total cost of a wind turbine system
$\gamma$	Coefficient of airfoil web thickness to airfoil skin thickness
$\lambda$	Tip speed ratio
$\rho$	Air density
$\sigma$	Stress
$\sigma_{sol}$	Solidity
$\tau$	Airfoil thickness
$\varphi$	Inflow angle

## References

1. Fingersh, L.; Hand, M.; Laxson, A. *Wind Turbine Design Cost and Scaling Model*; Technical Report; National Renewable Energy Laboratory (NREL): Golden, CO, USA, 2006.
2. Jonkman, J.; Butterfield, S.; Musial, W.; Scott, G. *Definition of a 5-MW Reference Wind Turbine for Offshore System Development*; Technical Report; National Renewable Energy Laboratory (NREL): Golden, CO, USA, 2009.
3. Jonkman, J.M.; Buhl, M.L., Jr. *FAST User's Guide*; Technical Report; National Renewable Energy Laboratory (NREL): Golden, CO, USA, 2005.
4. Gaertner, E.; Rinker, J.; Sethuraman, L.; Zahle, F.; Anderson, B.; Barter, G.; Abbas, N.; Meng, F.; Bortolotti, P.; Skrzypinski, W.; et al. *Definition of the IEA Wind 15-Megawatt Offshore Reference Wind Turbine*; Technical Report; National Renewable Energy Laboratory (NREL): Golden, CO, USA, 2020.
5. Bak, C.; Zahle, F.; Bitsche, R.; Kim, T.S.; Yde, A.; Henriksen, L.C.; Natarajan, A.; Hansen, M. *Description of the DTU 10 MW Reference Wind Turbine*; DTU Wind Energy Report-I-0092; Technical University of Denmark (DTU): Lyngby, Denmark, 2013.
6. Larsen, T.J.; Hansen, A.M. *How 2 HAWC2, the User's Manual*; Risø DTU National Laboratory: Roskilde, Denmark, 2019.
7. *IEC 61400-1*; Wind Energy Generation Systems—Part 1: Design Requirements. IEC: Geneva, Switzerland, 2019.
8. Bot, E.T.G.; Ceyhan, O. *Blade Optimisation Tool User's Manual*; The Energy Research Centre of the Netherlands (ECN): Petten, The Netherlands, 2009.
9. Montgomerie Jensen, B.O.G.; Brand, A.J.; Bosschers, J.; van Rooij, R.P.J.O.M. *Three-Dimensional Effects in Stall*; The Energy Research Centre of the Netherlands (ECN): Petten, The Netherlands, 1997.
10. Peeringa, J.; Brood, R.; Ceyhan, O.; Engels, W.; de Winkel, G. *UpWind 20MW Wind Turbine Pre-Design Blade Design and Control*; The Energy Research Centre of the Netherlands (ECN): Petten, The Netherlands, 2011.
11. Ashuri, T.; Martins, J.R.R.A.; Zaaijer, M.B.; van Kuik, G.A.M.; van Bussel, G.J.W. Aerosevoelastic Design Definition of a 20 MW Common Research and Turbine Model. *Wind. Energy* **2016**, *19*, 2071–2087. [[CrossRef](#)]
12. Ananda, G.K.; Bansal, S.; Selig, M.S. Aerodynamic Design of the 13.2 MW SUMR-13i Wind Turbine Rotor. In Proceedings of the 2018 Wind Energy Symposium, Kissimmee, FL, USA, 8–12 January 2018. [[CrossRef](#)]
13. Pao, L.Y.; Zalkind, D.S.; Griffith, D.T.; Chetan, M.; Selig, M.S.; Ananda, G.K.; Bay, C.J.; Stehly, T.; Loth, E. Control co-design of 13 MW Downwind Two-bladed Rotors to Achieve 25% Reduction in Levelized Cost of Energy. *Annu. Rev. Control* **2021**, *51*, 331–343. [[CrossRef](#)]
14. Qin, C.; Loth, E.; Zalkind, D.S.; Pao, L.Y.; Yao, S.; Griffith, D.T.; Selig, M.S.; Damiani, R. Downwind Coning Concept Rotor for a 25 MW Offshore Wind Turbine. *Renew. Energy* **2020**, *156*, 314–327. [[CrossRef](#)]
15. Yao, S.; Chetan, M.; Griffith, D.T.; Mendoza, A.S.E.; Selig, M.S.; Martin, D.; Kianbakht, S.; Johnson, K.; Loth, E. Aero-structural Design and Optimization of 50 MW Wind Turbine with over 250-m Blades. *Wind. Eng.* **2021**, *46*, 273–295. [[CrossRef](#)]
16. *Innovative Wind Conversion Systems (10–20 MW) for Offshore Applications*; Final Report Summary—INNWind.EU, 7th Framework Project, CORDIS; European Commission: Luxembourg, 2018. Available online: <https://cordis.europa.eu/project/id/308974/reporting> (accessed on 11 December 2018).
17. Jensen, P.H.; Chaviaropoulos, T.; Natarajan, A. *LCoE Reduction for the Next Generation Offshore Wind Turbine*; Outcomes from the INNWind.EU Project; European Commission: Luxembourg, 2017.
18. Kesikbaş, O. Investigations of Upscaling Effects for Aerodynamic Design of Large Wind Turbine Rotors by Using Bem Theory and Optimization. Master's Thesis, Middle East Technical University, Ankara, Turkiye, 2019.
19. Shafiee, M.; Brennan, F.; Espinosa, I.A. A Parametric Whole Life Cost Model for Offshore Wind Farm. *Int. J. Life Cycle Assess.* **2016**, *21*, 961–975. [[CrossRef](#)]
20. Griffith, D.T.; Johanns, W. *Large Blade Manufacturing Cost Studies Using the Sandia Blade Manufacturing Cost Tool and Sandia 100-Meter Blades*; SANDIA REPORT; Sandia National Laboratories: Albuquerque, NM, USA, 2013.

21. Ashuri, T. Beyond Classical Upscaling: Integrated Aeroservoelastic Design and Optimization of Large Offshore Wind Turbines. Ph.D. Thesis, Delft University of Technology, Zuid-Holland, The Netherlands, 2012.
22. Ashuri, T.; Zaaijer, M.B.; Martins, J.R.R.A.; van Bussel, G.J.W.; van Kuik, G.A.M. Multidisciplinary Design Optimization of Offshore Wind Turbines for Minimum Levelized Cost of Energy. *Renew. Energy* **2014**, *68*, 893–905. [[CrossRef](#)]
23. Serafeim, G.; Manoas, D.; Riziotis, V.; Chaviaropoulos, P. Multidisciplinary Aeroelastic Optimization of a 10 MW-scale Wind Turbine Rotor Targeting to Reduced LCoE. *J. Phys. Conf. Ser.* **2022**, *2265*, 042051. [[CrossRef](#)]
24. Bortolotti, P.; Berry, D.; Murray, R.; Gaertner, E.; Jenne, D.; Damiani, R.; Barter, G.; Dykes, K. *A Detailed Wind Turbine Blade Cost Model*; Technical Report; National Renewable Energy Laboratory (NREL): Golden, CO, USA, 2019.
25. Kannan, B.; Jeyyaraj, B. *Low Specific Power Wind Turbines for Reduced Levelized Cost of Energy*; IntechOpen: London, UK, 2022.
26. Hansen, M.O.L. *Aerodynamics of Wind Turbine*, 2nd ed.; EARTHSCAN: London, UK, 2008.
27. Jang, K.H. 20 MW Class Low-Induction Rotor Shape Design and Analysis for LCoE Reduction. Master's Thesis, Jeonbuk National University, Jeonju, Republic of Korea, 2023.
28. Chaviaropoulos, P.K.; Chortis, D.; Lekou, D. *Definition of the Reference Wind Turbine—Analysis of Rotor Design Parameters*; INNWIND.EU Project, Deliverable 1.2.1; European Commission: Luxembourg, 2013.
29. Giguère, P.; Selig, M.S.; Tangler, J.L. Blade Design Trade-Offs Using Low-Lift Airfoils for Stall-Regulated HAWTs. *J. Sol. Energy Eng.* **1999**, *121*, 217–223. [[CrossRef](#)]
30. Giguère, P.; Selig, M.S. Blade Geometry Optimization for the Design of Wind Turbine rotors. In Proceedings of the 2000 ASME Wind Energy Symposium, AIAA-2000-0045, 2000 ASME Wind Energy Symposium, Reno, NV, USA, 10–13 January 2000. [[CrossRef](#)]
31. Hibbeler, R.C. *Mechanics of Materials*, 9th ed.; PEARSON: London, UK, 2013.
32. Ryu, K.W.; Seo, Y.S.; Jeon, H.M.; Cho, H.S.; Park, S.Y.; Jang, K.H.; Choi, J.H.; Song, P.M.; Jung, I.H.; Cheon, S.W.; et al. *Conceptual Design for 20 MW Class Offshore Wind Power System around Korean Peninsula*; R21XO01-6; Korea Electric Power Corporation: Naju-si, Republic of Korea, 2022.
33. Ryu, K.W.; Jang, K.H. Aerodynamic Design and Loads Analysis for 20 MW Offshore Wind Turbine System. In Proceedings of the 2022 Spring Conference of Korea Wind Energy Association, Jeju, Republic of Korea, 20–22 June 2022.
34. Desmond, C.; Murphy, J.; Blonk, L.; Haans, W. Description of an 8 MW Reference Wind Turbine. *J. Phys. Conf. Ser.* **2016**, *753*, 92013. [[CrossRef](#)]
35. Schepers, J.G.; Ceyhan, O.; Savenije, F.J.; Stettner, M.; Kooijman, H.J.; Chaviaropoulos, P.; Sieros, G.; Simao Ferreira, C.; Sørensen, N.; Wächter, M.; et al. AVATAR: AdVanced Aerodynamic Tools for Large Rotors. In Proceedings of the 33rd Wind Energy Symposium, Kissimmee, FL, USA, 5–9 January 2015. [[CrossRef](#)]
36. Oh, K.Y.; Kim, J.Y.; Lee, J.S.; Ryu, K.W. Wind resource assessment around Korean Peninsula for feasibility study on 100 MW offshore wind farm. *Renew. Energy* **2012**, *42*, 217–226. [[CrossRef](#)]
37. Selig, M.S. *PROPID User Manual*; University of Illinois at Urbana-Champaign: Champaign, IL, USA, 2012.
38. Jang, K.H.; Ryu, K.W. Blade Shape Design with Minimization of LCoE. In Proceedings of the 2022 Spring Conference of Korea Wind Energy Association, Jeju, Republic of Korea, 20–22 June 2022.
39. Bortolotti, P.; Tarrés, H.C.; Dykes, K.; Merz, K.; Sethuraman, L.; Verelst, D.; Zahle, F. *Systems Engineering in Wind Energy WP2.1 Reference Wind Turbines*; Technical Report; IEA Wind; National Renewable Energy Laboratory: Oak Ridge, TN, USA, 2019.
40. Griffith, D.T.; Ashwill, T.D. *The Sandia 100-Meter All-Glass Baseline Wind Turbine Blade: SNL 100-00*; SANDIA REPORT; Sandia National Laboratories: Albuquerque, NM, USA, 2011.
41. Chaviaropoulos, P.; Sieros, G. Design of low induction rotors for use in large offshore wind farms. In Proceedings of the Scientific Track, European Wind Energy Association (EWEA), Barcelona, Spain, 10–13 March 2014.
42. Bergami, L.; Madsen, H.A.; Rasmussen, F. A two-bladed teetering hub configuration for the DTU 10 MW RWT: Loads considerations. In Proceedings of the EWEA 2014, Barcelona, Spain, 10–13 March 2014.

**Disclaimer/Publisher's Note:** The statements, opinions and data contained in all publications are solely those of the individual author(s) and contributor(s) and not of MDPI and/or the editor(s). MDPI and/or the editor(s) disclaim responsibility for any injury to people or property resulting from any ideas, methods, instructions or products referred to in the content.